Nanoscale

Accepted Manuscript

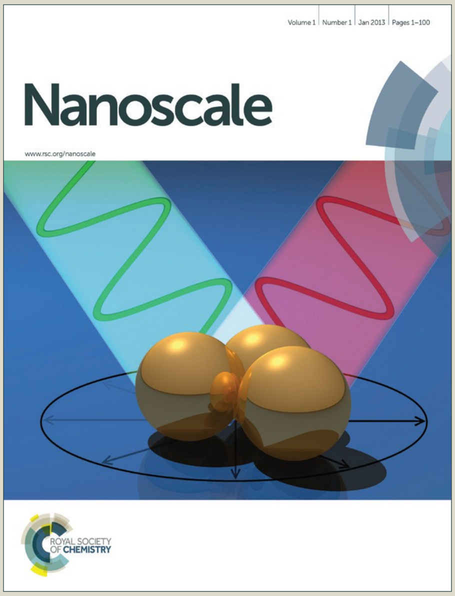

ROYAL SOCIETY OF CHEMISTRY

www.rsc.org/nanoscale

Ordered Mesoporous NiO with Thin Pore Walls and Their Enhanced Sensing Performance for Formaldehyde

Xiaoyong Lai,[a,b] Guoxin Shen,[a,b] Ping Xue,*[a,b] Bingqin Yan,[a,b] Hong Wang,[c] Peng Li [a], Weitao Xia [a]*
and Junzhuo Fang [a]

[a] Key Laboratory of Energy Resource and Chemical Engineering, State Key Laboratory Cultivation Base of Natural Gas Conversion, Ningxia University, Yinchuan 750021, People's Republic of China.

[b] School of Chemistry and Chemical Engineering, Ningxia University, Yinchuan 750021, People's Republic of China

[c] Department of Materials and Chemical Engineering, Sichuan University of Science and Engineering, Key Laboratory of Material Corrosion and Protection of Sichuan Province, Zigong, 643000, People's Republic of China

RECEIVED DATE

TITLE RUNNING HEAD: Mesoporous NiO based gas sensor.

CORRESPONDING AUTHOR FOOTNOTE:

Fax: +86 951 2062323; Tel: +86 951 2062861; E-mail: xylai@nxu.edu.cn; ping@nxu.edu.cn

Abstract

A class of formaldehyde (HCHO) gas sensors with high response were developed based on ordered mesoporous NiO, which were synthesized via the nanocasting route by directly using mesoporous silica as hard template. A series of mesoporous NiO with different textural parameters such as specific surface area, pore size, pore wall thickness, were attained by selecting mesoporous silica with different pore sizes as templates. The gas sensing properties for formaldehyde (HCHO) of the NiO specimens were examined. The results exhibit those mesoporous NiO possess much higher response to HCHO even at low concentration levels than the bulk NiO, and larger specific surface area and pore size as well as thinner pore walls would be benefit for enhancing the sensing properties of NiO.

KEYWORDS: Mesoporous; nickel oxide; nanocasting; gas sensor; formaldehyde.

Introduction

Ordered mesoporous metal oxides have attracted great interest in areas including catalysis,[1-5] gas sensor,[6-10] energy conversion and storage,[11-17] since the ordered periodical structure and large specific surface area allow for improved performances.[18-24] The conventional "soft template" method results in mesoporous materials with amorphous or semi-crystalline walls in most cases,[25, 26] which could limit their wider application. Recently, the nanocasting method, pioneered by Ryoo and coworkers,[27] has been adapted to prepare ordered mesoporous metal oxides with crystalline walls by ordered mesoporous silica or carbon as hard templates, such as TiO_2, Cr_2O_3, MnO_x, Fe_2O_3, Co_3O_4, NiO, CuO, ZnO, ZrO_2, In_2O_3, SnO_2, CeO_2, WO_3.[28-47] In this method, suitable precursors are introduced into the pores of mesoporous templates. Subsequent heating to obtain the desired crystalline metal oxides and selective removal of the template could leave a negative mesoporous metal oxide replica and the topological structure, pore size and wall thickness of the resultant replica could be to some degree tuned by correspondingly changing those of their templates.[8, 15, 48-51]

Nickel oxide (NiO), a wide bandgap (3.6~4.0 eV) *p*-type semiconductor with high thermal stability and unique magnetic, optical, and electrical properties, was found to be effective for some applications in the fields of gas sensors,[52-55] magnetism,[56] catalysis,[57] and lithium ion batteries.[58-60] Although some ordered mesoporous NiO materials have been reported in preparation,[28, 30, 61] studies on systemically investigating their potential applications have been limited. Liu et al.[16] reported the improved performance of ordered mesoporous NiO as the anode material for lithium ion batteries and Wahab et al.[62] also demonstrated the availability of ordered mesoporous NiO for the immobilization of proteins. However, to the best of our knowledge, there has been no report about highly ordered mesoporous NiO for gas sensors. Ordered mesoporous NiO materials have lots of advantages in the application of gas sensors compared to their bulk counterparts, whose regular porosity and large specific surface area would permit high accessibility for the gas molecules and provide more active sites for the surface-chemical interaction between the gas molecules and NiO materials. Additionally, their pore walls are in nanoscale dimension and thus large proportion of carriers in sensing materials could be affected by the above-mentioned surface-chemical interaction, resulting in a high sensing response.

Ordered mesoporous NiO materials with controlled pore wall thicknesses were synthesized via the nanocasting route by using mesoporous silica KIT-6 as template. It is known that KIT-6 exhibit 3D bicontinuous network of large channels with interconnecting micropores and small mesopores and that the size of large channels and pore interconnectivity could be controlled by adjusting the hydrothermal aging temperature.[34, 63] A series of mesoporous NiO with different textural parameters such as specific surface area, pore size, pore wall thickness, were attained by selecting mesoporous silica obtained at different hydrothermal aging temperature as templates. The gas sensing properties for formaldehyde (HCHO) of the NiO specimens were investigated. The results exhibit those mesoporous NiO possess much higher response to HCHO even at low concentration levels than their bulk counterparts, and larger specific surface area and pore size as well as thinner pore walls would be benefit for enhancing the sensing properties of NiO.

Experimental

Synthesis. Mesoporous silica were prepared under hydrothermal synthesis temperature of 40, 80 and 130 °C for 24 h, according to the established procedures.[64] The template was removed by calcination at 500 °C. The resultant silica species were referred to as KIT-6-*x*, where *x* stands for the hydrothermal aging temperature. Mesoporous NiO could be prepared by using the above-mentioned mesoporous silica (KIT-6-*x*) as hard template, referred to as NiO-*x*. Typically, 1.2 g of KIT-6-*x* was dispersed in 10 g of ethanol solution containing 1.968 g of $Ni(NO_3)_2 \cdot 6H_2O$ precursor and then stirred at 40 °C until that ethanol was evaporated. Afterward, the resulting powder was heated in a ceramic crucible in an oven at 300 °C for 4 h, in order to decompose $Ni(NO_3)_2 \cdot 6H_2O$. The filling and heating steps were repeated once following the same conditions in order to achieve higher loadings, except for the amounts of $Ni(NO_3)_2 \cdot 6H_2O$ were decreased to 1.418 g. Finally, the silica template was then removed at room temperature using a 2 M NaOH aqueous solution. The black NiO material was recovered by centrifugation and dried at 70 °C overnight. Moreover, bulk NiO particles were also prepared by directly decomposing $Ni(NO_3)_2 \cdot 6H_2O$ without templates at 800 °C.

Characterization. The powder X-ray diffraction (XRD) patterns were recorded with a Bruker AXS D8 diffractometer (Cu Kα (λ=1.5405 Å radiation) operating with 40 mA and 40 kV. Scanning electron microscopy (SEM) images were obtained with a KYKY-2800B, operating at 25 kV. Transmission electron microscopy (TEM) images were recorded with a JEOL JEM-2100F, operating at an acceleration voltage of 200 kV. N_2 physisorption isotherms at the temperature of liquid nitrogen (77 K) were measured on an ASAP 2020 HD adsorption analyzer (Micromeritics) with prior degassing under vacuum at 200 °C for 4h. Total pore volumes were determined using the adsorbed volume at a relative pressure of 0.99. Multipoint Brunauer-Emmet-Teller (BET) surface area was estimated from the relative pressure range of 0.05 ~ 0.2. The pore size distributions of all mesostructured materials were calculated from the adsorption branches of the N_2 physisorption isotherms using the Barrett-Joyner-Halenda (BJH) algorithm except for mesoporous silica materials, for which nonlocal density functional theory (NLDFT) methods were used.

Sensing Test. Sensors were fabricated by coating the samples on an interdigital electrode as a sensing layer and the testing principle were similar to that for previous report:[9, 65] 2 mg of NiO samples were dispersed in 1 mL of water under ultrasonic and 5 μL of the resultant suspension (2 $mg \cdot mL^{-1}$) was dropped on the interdigital electrode. After the evaporation of water, NiO sensing layer formed on the interdigital electrode and was heated at 300 °C for 1h. The sensor was placed in a tube furnace to provide the work temperature. Formaldehyde was introduced into the quartz tube by bubbling its aqueous solution (0, 0.001, 0.005, 0.01, 0.1, 0.5, 1 and 5 wt%) using air flow with a speed of 600 sccm, whose concentration in gaseous phase was detected via acetylacetone spectrophotometric method to be 0, 0.2, 0.7, 1, 9, 46, 90, 380 ppm. The electrical response of the sensor was measured with an automatic test system, controlled by a personal computer (see the ESI, Fig. S1).

Results and Discussion

The ordered mesoporous silica materials (KIT-6-*x*), with the 3D cubic *Ia3d* symmetry and different pore sizes, were used as the templates for the synthesis of ordered mesoporous NiO materials (NiO-*x*). Fig. 1 shows the low-angle XRD patterns and nitrogen physisorption isotherms for the KIT-6-*x* mesoporous silica templates. Low-angle XRD patterns of all the mesoporous silica templates (shown in Fig. 1A) display an intense diffraction peak indexed as the (211) reflection of the 3D cubic *Ia3d* symmetry, which are gradually shifted to the lower angle region with increasing the hydrothermal synthesis temperature from 40 to 130 °C. This peak shifting phenomenon is related to the difference of lattice shrinkage of mesoporous silica templates during calcination. The nitrogen physisorption isotherms of the KIT-6 silica materials are shown in Fig. 1B, synthesized at different hydrothermal synthesis temperatures with the type-IV hysteresis loop in the relative pressure range of 0.5 ~ 0.8 that are characteristic of the mesoporous material. KIT-6-*x* contains two sets of interpenetrating mesopores, which are bridged by some secondary pores within their walls. The corresponding pore size distributions are shown in the inset of Fig. 1B. As the hydrothermal aging temperatures increases from 40 to 130 °C, the mesopore sizes gradually increased from 5.7 to 9.4 nm, companied by the enlarging of secondary pores, but pore wall thicknesses calculated by the method in the literature,[34] decreased from 3.6 to 2.6 nm. Total pore volumes of KIT-6 were also gradually increased from 0.68 to 0.96 $cm^3 \cdot g^{-1}$ with increasing the hydrothermal aging temperature (Table 1). These results suggest that relatively high temperature hydrothermal treatment could indeed enlarge not only the primary mesopore of silica but also the secondary pore within the silica walls and improve its pore interconnectivity.[9, 66]

Fig. 2 shows the low-angle XRD patterns and nitrogen physisorption isotherms for ordered mesoporous NiO materials (NiO-*x*). Low-angle XRD patterns of all the mesoporous NiO materials (shown in Fig. 2A) display an intense diffraction peak indexed as the (211) reflection of the 3D cubic *Ia3d* symmetry, suggesting the ordered mesostructure replication from mesoporous silica template KIT-6 to NiO replica, although the higher order diffraction peaks [(220) and (332)] were invisible in the low-angle XRD patterns of NiO-40 and NiO-80, suggesting a decrease of ordered mesostructure during replication. All of the NiO materials exhibit typical type-IV isotherms with a hysteresis loop, which are characteristic of the mesoporous material. The corresponding pore size distributions are shown in Fig. 3. The first peak at 3.7, 3.7, and 3.3 nm for NiO-40, NiO-80, and NiO-130 respectively is consistent with the wall thickness of their templates (Table 1). Correspondingly, their wall thickness could be estimated to be 5.1, 6.5 and 8.5 nm by the method in the literature,[34] which is in agreement with the pore size of their templates.

Moreover, there is also another peak at 12 nm for NiO-40 and NiO-80, but not NiO-130. Generally, NiO growing in KIT-6 with high pore interconnectivity could cut across two sets of mesopores via secondary pores and produce a coupled subframework with a pore size equivalent to the template wall thickness, whereas NiO tends to only grow within one of two sets of mesopores in those templates with low pore interconnectivity and generate a uncoupled subframework with a larger pore size equivalent to the sum of two wall thicknesses and a pore size of the template.[61] Therefore, we conclude that NiO-40 and NiO-80 consists of both the coupled and uncoupled subframework structures, which could also be confirmed by TEM images (Fig. 4b and 4c). The ratio of small pores to large pores, i.e. the ratio of the coupled and uncoupled subframework, is proportion to the pore interconnectivity of their templates.

TEM observations, as shown in Fig. 4, reveals highly ordered mesostructure of all the NiO replicas almost throughout the whole particle domain and the secondary particles with the size between 100~200 nm. In the NiO-40 and NiO-80, uncoupled subframeworks could be observed on the edges with large-pore domains (Fig. 4b and 4c), confirming the above-mentioned deduction. Wide-angle powder X-ray diffraction patterns of all the mesoporous NiO are shown in Fig. 5. Three well-resolved peaks were observed, which could be indexed as to (111), (200), (220) planes of the standard cubic bunsenite mineral structure (JPCDS No. 89-7390), and no peaks of other impurities are observed.

Formaldehyde (HCHO) is a well-known hazardous air pollutant and the effective methods for detecting HCHO are of great importance.[67-70] The potential application of ordered mesoporous NiO in gas sensor was investigated for HCHO detection. The response of gas sensors fabricated by ordered mesoporous NiO to 380 ppm HCHO in air was tested as a function of operating temperature. Here, the sensor response (sensitivity) was defined as and the ratio of resistance in air containing HCHO gas (R_{gas}) and that in air (R_{air}). The response of the NiO-40 based sensor to HCHO increases with the operating temperature up to a maximum value located at about 300 °C and then decreases if further increasing the operating temperature (see the ESI, Fig. S2). The principle of semiconductor gas sensor is mainly based on a change in electrical conductivity resulting from adsorption and desorption of gas molecules on the surface of sensing materials. When NiO is placed in air, oxygen molecules absorbed on its surface will capture electrons from its conduction band to generate chemisorbed oxygen species (O_2^-, O^- and O^{2-}), which results in the increase of hole concentration in NiO and conductivity. When HCHO is introduced, it will react with the oxygen species and the captured electron will be released back to the conduction band, leading to a decrease of hole concentration in NiO and conductivity. When the operating temperature increases, oxygen molecules absorbed on the surface of NiO will capture more electrons from its conduction band to generate chemisorbed oxygen species (O_2^-, O^- and O^{2-}), and thus a higher response is observed. However, chemisorbed oxygen species would tend to drop from the surface of semiconductor as further increasing temperature, thus resulting in a lower response. Therefore the optimum operating temperature is 300 °C, and all further tests would be performed at this temperature.

The dynamic response curves to HCHO for all the sensors are depicted in Fig. 6. Response and recovery times of all the sensors (defined as the time to reach 90% of the final equilibrium value) are calculated from the case of 380 ppm HCHO, which depend largely upon the diffusion of HCHO within the sensing layer. Knudsen diffusion is the main diffusion type for the smaller pore (several nanometers), which gives a diffusion coefficient depending linearly on the pore size.[71] As a result, the diffusion of HCHO in mesoporous NiO with relatively small pores, which exhibits longer response and recovery time (119 and 39 s, 188 and 77 s, 196 and 80 s for NiO-40, NiO-80, NiO-130, respectively), compared with that of bulk NiO particles (48 and 29 s) with larger inter-particle textural pores. Moreover, the response and recovery time for NiO-40 with more additional larger mesopores (12 nm) is shorter than those for other two mesoporous NiO samples, which suggests that large pores would benefit the diffusion of HCHO in sensing layer and improve the response speed of the sensors.

Fig. 7 shows the correlation between the response of all the sensors and the concentration of HCHO. We could observe that all the sensors fabricated from mesostructured NiO, especially NiO-40, displayed a higher response to HCHO in whole testing concentration range (0.2~380 ppm) than that from bulk NiO particle (3 $m^2 \cdot g^{-1}$), which is attributed to the former's high surface area that allow them absorb more gas molecules and thus more sensitive. Even if compared with those NiO based HCHO sensors reported in previous literatures,[72-76] NiO-40 based sensor still possesses the considerable advantage in response (see the ESI, Table S1). However, we also note that the response of those mesoporous NiO sensors is not exactly proportional to their surface areas. The response of NiO-40 with a specific surface area of 109 $m^2 \cdot g^{-1}$ exhibits a higher response of 20.6 to 380 ppm HCHO, than those of other two mesoporous NiO samples (12.6 and 11.5 for NiO-80 and NiO-130) with similar specific surface areas (118 $m^2 \cdot g^{-1}$ and 81 $m^2 \cdot g^{-1}$). Furthermore, NiO nanoparticles with a large specific surface area of 185 $m^2 \cdot g^{-1}$ and a size of ~5 nm were also used as sensing material, which exhibited a weaker response of 5.9 to 380 ppm HCHO (see the ESI, Fig. S3-5). The response of NiO based gas sensor is mainly determined on a change in electrical conductivity resulting from the adsorption of oxygen and the reaction of pre-adsorbed oxygen species and HCHO on its surface. Oxygen molecules absorbed on its surface will capture electrons from NiO to generate chemisorbed oxygen species (O_2^-, O^- and O^{2-}), resulting in the formation of high conductive hole accumulation layer and the increase of electrical conductivity, whereas HCHO could react with the oxygen species and then the captured electron will recombine with holes, leading to an decrease in electrical conductivity. Barsan et al have proposed a core-shell model composed of high conductive hole accumulation layer and low conductive inner core for large *p*-type semiconductor particles and demonstrated that the slight change in the concentration of hole in accumulation layer due to electron–hole recombination will not lead to significant variation in the conductivity.[77] When the size of NiO is closed to and even less than twice the thickness of hole accumulation layer (which corresponds to its Debye length L_D of ~3nm),[76, 78] a high fraction of sensing layer will be involved in the charge transfer process, which will result in a strong response. Du et al. also reported that the sensor response of NiO nanoparticles gradually increases with reducing the particle size from 31.5 to 11.5 nm.[79] Therefore, the poor response of bulk NiO particles with micrometer sizes is expectable. However, there is no available model for nanoscaled nongranular *p*-type semiconductor, especially those with a size close to or less than $2L_D$. By analogy with nanoparticles, we can imagine that both the conduction channel along the pore walls of mesoporous NiO and inner core are very thin. For example, the pore wall thicknesses for NiO-80 and NiO-130 are 6.5 and 8.5 nm and the corresponding thicknesses of their inner cores are only 0.5 and 2.5 nm. Therefore, the hole concentration in both them could be easily affected by the surface reaction of HCHO and oxygen species, thus resulting in a high response. Especially, NiO-40 has a thinnest pore wall of 5.1 nm, which means the hole accumulation layer extend to the whole pore wall (Fig. 8) and the hole concentration and the conductivity would completely be controlled by gas exposure and thus NiO-40 exhibits a very strong response to HCHO. Moreover, the response is also related to the thickness of sensing layer and the diffusion of gas molecules within sensing layer. Castro-Hurtado et al. reported that NiO thin film with 150 nm thickness have better response than the thicker ones.[80] The typical thickness of NiO-40 sensing layer is about 1.8 μm (see the ESI, Fig. S6) at the given coating condition. When the coating procedure was repeated twice, the response of the resultant thicker NiO-40 film based sensor significantly decreased indeed (see the ESI, Fig. S7), since the diffusion of gas molecules within thicker sensing layer would be limited and gas exposure could only involve partial sensing layer, thus resulting in a low response. Compared with mesoporous NiO especially NiO-40 with more additional large pore, which could facilitate the gas diffusion, NiO nanoparticles with smaller size trend to aggregate, easily surfer from grain growth and form relatively dense sensing layer, which will result in a poor gas diffusion and low response. Similar results are also observed in the cases of In_2O_3 nanoparticles and their mesoporous counterparts.[9] In addition, the stability of NiO-40 sensor was primarily tested and there is no significant decrease in the response of NiO-40 based sensor to 380 ppm HCHO during three consecutive cycles (Fig. 6A), which could still keep 80% of response after half a year (see the ESI, Fig. S8). Considering no any stabilizer was used in the sensing layer, those results should be acceptable and further improvement is still ongoing.

Conclusion

Ordered mesoporous NiO were synthesized by directly using mesoporous silica as template via the nanocasting route. A series of mesoporous NiO replicas with controlled textural properties were attained by selecting mesoporous silica with different pore sizes as templates. The response towards HCHO of the resultant ordered mesoporous NiO with thin pore walls were found to be very strong even at relatively lower levels and such materials are useful in detecting HCHO. The gas sensing properties of mesostructured sensors prove to be affected by their textural parameters such as specific surface area, pore wall thickness, pore size.

ACKNOWLEDGMENT

This work was partly supported by the National Natural Science Foundation of China (No. 51362024, 21006116 and 51272165), the Natural Science Foundation of Ningxia of China (No. NZ12111) the Prophase Research Special Project of 973 (No. 2012CB723106), the Chinese Ministry of Science & Technology. X.Y.L. thanks the West Light Foundation of The Chinese Academy of Sciences.

Supporting Information Available: Gas sensor testing details, temperature-dependent response curves of NiO-40 based sensor, preparation, characterization and HCHO sensing of NiO nanoparticles, photograph of NiO sensor and SEM images of its cross section and comparison of response of various HCHO sensors.

Reference

1. H. Tuysuz, M. Comotti and F. Schuth, *Chem. Commun.*, 2008, 4022-4024.
2. J. K. Zhu, Q. M. Gao and Z. Chen, *Appl. Catal. B*, 2008, **81**, 236-243.
3. J. K. Zhu and Q. M. Gao, *Microporous Mesoporous Mater.*, 2009, **124**, 144-152.
4. C. Y. Ma, Z. Mu, J. J. Li, Y. G. Jin, J. Cheng, G. Q. Lu, Z. P. Hao and S. Z. Qiao, *J. Am. Chem. Soc.*, 2010, **132**, 2608-2613.
5. D. Gu, C. J. Jia, H. Bongard, B. Spliethoff, C. Weidenthaler, W. Schmidt and F. Schuth, *Appl. Catal. B*, 2014, **152**, 11-18.
6. E. Rossinyol, A. Prim, E. Pellicer, J. Arbiol, F. Hernandez -Ramirez, F. Peiro, A. Cornet, J. R. Morante, L. A. Solovyov, B. Z. Tian, T. Bo and D. Y. Zhao, *Adv. Funct. Mater.*, 2007, **17**, 1801-1806.
7. A. Prim, E. Pellicer, E. Rossinyol, F. Peiro, A. Cornet and J. R. Morante, *Adv. Funct. Mater.*, 2007, **17**, 2957-2963.
8. T. Waitz, T. Wagner, T. Sauerwald, C. D. Kohl and M. Tiemann, *Adv. Funct. Mater.*, 2009, **19**, 653-661.
9. X. Y. Lai, D. Wang, N. Han, J. Du, J. Li, C. J. Xing, Y. F. Chen and X. T. Li, *Chem. Mater.*, 2010, **22**, 3033-3042.
10. X. H. Sun, H. R. Hao, H. M. Ji, X. L. Li, S. Cai and C. M. Zheng, *ACS Appl. Mater. Inter.*, 2014, **6**, 401-409.

11. J. Y. Luo, Y. G. Wang, H. M. Xiong and Y. Y. Xia, *Chem. Mater.*, 2007, **19**, 4791-4795.
12. F. Jiao and P. G. Bruce, *Adv. Mater.*, 2007, **19**, 657-660.
13. G. Wang, H. Liu, J. Horvat, B. Wang, S. Qiao, J. Park and H. Ahn, *Chem. Eur. J.*, 2010, **16**, 11020-11027.
14. Y. Ren, L. J. Hardwick and P. G. Bruce, *Angew. Chem. Int. Ed.*, 2010, **49**, 2570-2574.
15. Y. Ren, A. R. Armstrong, F. Jiao and P. G. Bruce, *J. Am. Chem. Soc.*, 2010, **132**, 996-1004.
16. H. Liu, G. Wang, J. Liu, S. Qiao and H. Ahn, *J. Mater. Chem.*, 2011, **21**, 3046-3052.
17. F. Jiao, H. Yen, G. S. Hutchings, B. T. Yonemoto, Q. Lu and F. Kleitz, *J. Mater. Chem. A*, 2013.
18. C. Z. Yu, B. Z. Tian and D. Y. Zhao, *Curr Opin Solid St M*, 2003, **7**, 191-197.
19. Y. Ren, Z. Ma and P. G. Bruce, *Chem. Soc. Rev.*, 2012, **41**, 4909-4927.
20. W. Li and D. Y. Zhao, *Chem. Commun.*, 2013, **49**, 943-946.
21. Y. Teng, L. X. Song, A. Ponchel, Z. K. Yang and J. Xia, *Adv. Mater.*, 2014, **26**, 6238-6243.
22. Y. Teng, L. X. Song, A. Ponchel, E. Monflier, Z. C. Shao, J. Xia and Z. K. Yang, *RSC Adv.*, 2014, **4**, 26847-26854.
23. A. Lannoy, R. Bleta, C. Machut, E. Monflier and A. Ponchel, *RSC Adv.*, 2014, **4**, 40061-40070.
24. R. Bleta, A. Lannoy, C. Machut, E. Monflier and A. Ponchel, *Langmuir*, 2014, **30**, 11812-11822.
25. B. Lee, D. L. Lu, J. N. Kondo and K. Domen, *Chem. Commun.*, 2001, 2118-2119.
26. J. N. Kondo and K. Domen, *Chem. Mater.*, 2008, **20**, 835-847.
27. S. Jun, S. H. Joo, R. Ryoo, M. Kruk, M. Jaroniec, Z. Liu, T. Ohsuna and O. Terasaki, *J. Am. Chem. Soc.*, 2000, **122**, 10712-10713.
28. B. Z. Tian, X. Y. Liu, H. F. Yang, S. H. Xie, C. Z. Yu, B. Tu and D. Y. Zhao, *Adv. Mater.*, 2003, **15**, 1370-1374.
29. S. C. Laha and R. Ryoo, *Chem. Commun.*, 2003, 2138-2139.
30. B. Z. Tian, X. Y. Liu, L. A. Solovyov, Z. Liu, H. F. Yang, Z. D. Zhang, S. H. Xie, F. Q. Zhang, B. Tu, C. Z. Yu, O. Terasaki and D. Y. Zhao, *J. Am. Chem. Soc.*, 2004, **126**, 865-875.
31. Y. Q. Wang, C. M. Yang, W. Schmidt, B. Spliethoff, E. Bill and F. Schuth, *Adv. Mater.*, 2005, **17**, 53-56.
32. J. Roggenbuck and M. Tiemann, *J. Am. Chem. Soc.*, 2005, **127**, 1096-1097.
33. F. Jiao, A. Harrison, J. C. Jumas, A. V. Chadwick, W. Kockelmann and P. G. Bruce, *J. Am. Chem. Soc.*, 2006, **128**, 5468-5474.
34. A. Rumplecker, F. Kleitz, E. L. Salabas and F. Schuth, *Chem. Mater.*, 2007, **19**, 485-496.
35. W. B. Yue and W. Z. Zhou, *J. Mater. Chem.*, 2007, **17**, 4947-4952.
36. Q. Liu, A. Q. Wang, X. D. Wang and T. Zhang, *Chem. Mater.*, 2006, **18**, 5153-5155.
37. X. Y. Lai, X. T. Li, W. C. Geng, J. C. Tu, J. X. Li and S. L. Qiu, *Angew. Chem. Int. Ed.*, 2007, **46**, 738-741.
38. J. Roggenbuck, H. Schafer, T. Tsoncheva, C. Minchev, J. Hanss and M. Tiemann, *Microporous Mesoporous Mater.*, 2007, **101**, 335-341.
39. S. Polarz, A. V. Orlov, F. Schuth and A. H. Lu, *Chem. Eur. J.*, 2007, **13**, 592-597.
40. T. Wagner, T. Waitz, J. Roggenbuck, M. Froba, C. D. Kohl and M. Tiemann, *Thin Solid Films*, 2007, **515**, 8360-8363.
41. L. Zhou, Q. J. Ren, X. F. Zhou, J. W. Tang, Z. H. Chen and C. Z. Yu, *Microporous Mesoporous Mater.*, 2008, **109**, 248-257.
42. H. Kim and J. Cho, *J. Mater. Chem.*, 2008, **18**, 771-775.
43. B. Liu and R. T. Baker, *J. Mater. Chem.*, 2008, **18**, 5200-5207.
44. H. Tuysuz, Y. Liu, C. Weidenthaler and F. Schuth, *J. Am. Chem. Soc.*, 2008, **130**, 14108-14110.
45. W. B. Yue, C. Randorn, P. S. Attidekou, Z. X. Su, J. T. S. Irvine and W. Z. Zhou, *Adv. Funct. Mater.*, 2009, **19**, 2826-2833.
46. M. B. Zheng, J. Cao, S. T. Liao, J. S. Liu, H. Q. Chen, Y. Zhao, W. J. Dai, G. B. Ji, J. M. Cao and J. Tao, *J. Phys. Chem. C*, 2009, **113**, 3887-3894.
47. X. Sun, Y. Shi, P. Zhang, C. Zheng, X. Zheng, F. Zhang, Y. Zhang, N. Guan, D. Zhao and G. D. Stucky, *J. Am. Chem. Soc.*, 2011, **133**, 14542-14545.

48. Y. Ren, F. Jiao and P. G. Bruce, *Microporous Mesoporous Mater.*, 2009, **121**, 90-94.
49. P. Shu, J. Ruan, C. Gao, H. Li and S. Che, *Microporous Mesoporous Mater.*, 2009, **123**, 314-323.
50. Z. Yang, Y. Lu and Z. Yang, *Chem. Commun.*, 2009, 2270-2277.
51. Y. Wang, Y. Wang, J. Ren, Y. Mi, F. Zhang, C. Li, X. Liu, Y. Guo, Y. Guo and G. Lu, *J. Solid State Chem.*, 2010, **183**, 277-284.
52. P. Rai, J. W. Yoon, H. M. Jeong, S. J. Hwang, C. H. Kwak and J. H. Lee, *Nanoscale*, 2014, **6**, 8292-8299.
53. F. Li, Y. Chen and J. Ma, *RSC Adv.*, 2014, **4**, 14201-14205.
54. C. H. Zhao, J. C. Fu, Z. X. Zhang and E. Q. Xie, *RSC Adv.*, 2013, **3**, 4018-4023.
55. P. V. Tong, N. D. Hoa, N. V. Duy, V. V. Quang, N. T. Lam and N. V. Hieu, *Int. J. Hydrogen Energy*, 2013, **38**, 12090-12100.
56. D. P. Chen, X. L. Wang, Y. Du, S. Ni, Z. B. Chen and X. Z. Liao, *Cryst. Growth Des.*, 2012, **12**, 2842-2849.
57. Q. Dong, S. Yin, C. S. Guo, X. Y. Wu, N. Kumada, T. Takei, A. Miura, Y. Yonesaki and T. Sato, *Appl. Catal., B*, 2014, **147**, 741-747.
58. Y. Q. Zhu, H. Z. Guo, Y. Wu, C. B. Cao, S. Tao and Z. Y. Wu, *J. Mater. Chem., A*, 2014, **2**, 7904-7911.
59. L. X. Liu, Y. Y. Guo, Y. P. Wang, X. J. Yang, S. X. Wang and H. Guo, *Electrochim. Acta*, 2013, **114**, 42-47.
60. G. P. Kim, S. Park, I. Nam, J. Park and J. Yi, *J. Power Sources*, 2013, **237**, 172-177.
61. F. Jiao, A. H. Hill, A. Harrison, A. Berko, A. V. Chadwick and P. G. Bruce, *J. Am. Chem. Soc.*, 2008, **130**, 5262-5266.
62. M. A. Wahab and F. Darain, *Nanotechnology*, 2014, **25**, 165701-165707.
63. L. H. Xing, J. H. Huang, S. J. Wu, H. S. Wang, K. Song, H. Y. Xu, Z. Q. Wang and Q. B. Kan, *Carbon*, 2007, **45**, 220-222.
64. F. Kleitz, S. H. Choi and R. Ryoo, *Chem. Commun.*, 2003, 2136-2137.
65. N. Han, Y. J. Tian, X. F. Wu and Y. F. Chen, *Sens. Actuators B*, 2009, **138**, 228-235.
66. M. Choi, W. Heo, F. Kleitz and R. Ryoo, *Chem. Commun.*, 2003, 1340-1341.
67. X. Y. Lai, P. Li, T. L. Yang, J. C. Tu and P. Xue, *Scripta Mater.*, 2012, **67**, 293-296.
68. Y. Zeng, X. L. Wang and W. T. Zheng, *J. Nanosci. Nanotech.*, 2013, **13**, 1286-1290.
69. T. Salthammer, *Angew. Chem. Int. Ed.*, 2013, **52**, 3320-3327.
70. D. Mao, J. X. Yao, X. Y. Lai, M. Yang, J. Du and D. Wang, *Small*, 2011, **7**, 578-582.
71. M. Tiemann, *Chem. Eur. J.*, 2007, **13**, 8376-8388.
72. L. L. Wang, Z. Lou, T. Fei and T. Zhang, *Sens. Actuators B*, 2012, **161**, 178-183.
73. G. X. Zhu, C. Y. Xi, H. Xu, D. Zheng, Y. J. Liu, X. Xu and X. P. Shen, *RSC Adv.*, 2012, **2**, 4236-4241.
74. M. Z. Liu, Y. P. Wang, P. C. Li, Z. Q. Cheng, Y. Q. Zhang, M. Y. Zhang, M. J. Hu and J. F. Li, *Appl. Surf. Sci.*, 2013, **284**, 453-458.
75. G. Li, X. Wang, H. Ding and T. Zhang, *RSC Adv.*, 2012, **2**, 13018-13023.
76. I. Castro-Hurtado, C. Malagu, S. Morandi, N. Perez, G. G. Mandayo and E. Castano, *Acta Mater.*, 2013, **61**, 1146-1153.
77. N. Barsan, C. Simion, T. Heine, S. Pokhrel and U. Weimar, *J. Electroceram.*, 2010, **25**, 11-19.
78. H. L. Chen, Y. M. Lu and W. S. Hwang, *Surf. Coat. Technol.*, 2005, **198**, 138-142.
79. Y. Du, W. N. Wang, X. W. Li, J. Zhao, J. M. Ma, Y. P. Liu and G. Y. Lu, *Mater. Lett.*, 2012, **68**, 168-170.
80. I. Castro-Hurtado, J. Herran, G. G. Mandayo and E. Castano, *Thin Solid Films*, 2011, **520**, 947-952.

TABLES.

Table 1 Textural Properties of Mesostructured Products.

Product	d_{211} (nm) [a]	Pore size (nm) [b]	Pore wall thickness (nm) [c]	BET specific surface area ($m^2 \cdot g^{-1}$)	Pore volume ($cm^3 \cdot g^{-1}$)
KIT-6-40	7.6	5.7	3.6	740	0.52
NiO-40	7.2	3.7(12)	5.1	109	0.51
KIT-6-80	8.5	7.3	3.1	878	0.76
NiO-80	8.3	3.7(12)	6.5	118	0.50
KIT-6-130	9.8	9.4	2.6	720	0.96
NiO-130	9.6	3.3	8.5	81	0.23

[a] d_{211}-spacing (d_{211}) of the materials was obtained from the low angle XRD patterns using Bragg's equation.

[b] Pore size (D_p)was calculated from the desorption branches of the N_2 physisorption isotherms using the Barrett-Joyner-Halenda (BJH) algorithm except for mesoporous silica materials, for which nonlocal density functional theory (NLDFT) methods were used.

[c] Pore wall thickness (T_w) was calculated by using the equation,[34] $T_w = d_{211}\sqrt{6}/2-D_p$

Figure captions:

Fig. 1 (A) Low-angle XRD patterns and (B) nitrogen physisorption isotherms of (a) KIT-6-40, (b) KIT-6-80 and (c) KIT-6-130. Inset in (B) shows the corresponding pore size distributions.

Fig. 2 (A) Low-angle XRD patterns and (B) nitrogen physisorption isotherms of (a) NiO-40, (b) NiO-80 and (c) NiO-130.

Fig. 3 Pore size distributions of (a) NiO-40, (b) NiO-80 and (c) NiO-130.

Fig. 4 TEM images of (a, b) NiO-40, (c) NiO-80 and (d) NiO-130.

Fig. 5 Wide-angle XRD patterns of (a) NiO-40, (b) NiO-80 and (c) NiO-130.

Fig. 6 Typical dynamic response curves of gas sensors fabricated from (A) NiO-40, (B) NiO-80, (C) NiO-130 and (D) bulk NiO particle, during cycling between increasing concentration of HCHO and ambient air at 300 °C.

Fig. 7 Response versus HCHO concentration of gas sensors fabricated from (a) NiO-40, (b) NiO-80, (c) NiO-130, (d) bulk NiO particle.

Fig. 8 Illustration of the dependence of the response on the textural parameters of the sensing material.

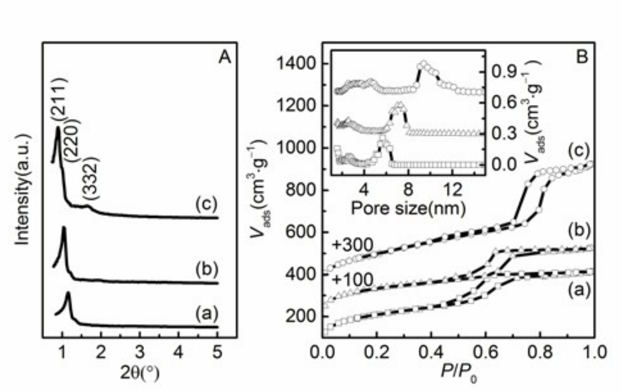

Fig. 1 (A) Low-angle XRD patterns and (B) nitrogen physisorption isotherms of (a) KIT-6-40, (b) KIT-6-80 and (c) KIT-6-130. Inset in (B) shows the corresponding pore size distributions.

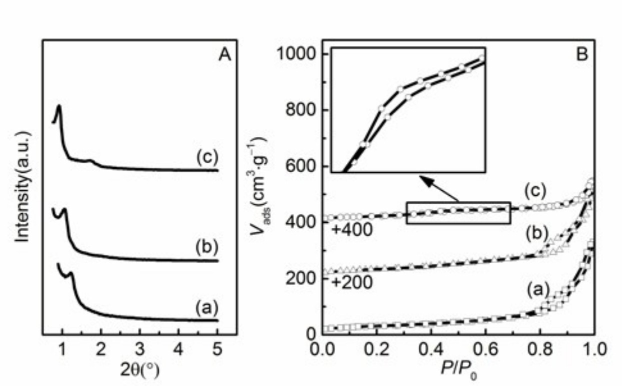

Fig. 2 (A) Low-angle XRD patterns and (B) nitrogen physisorption isotherms of (a) NiO-40, (b) NiO-80 and (c) NiO-130.

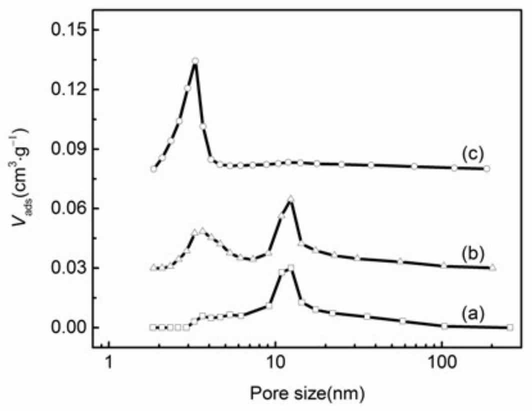

Fig. 3 Pore size distributions of (a) NiO-40, (b) NiO-80 and (c) NiO-130.

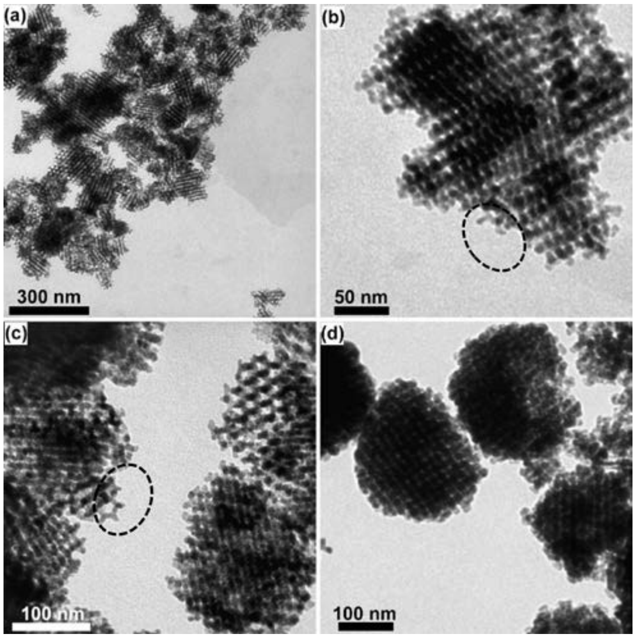

Fig. 4 TEM images of (a, b) NiO-40, (c) NiO-80 and (d) NiO-130.

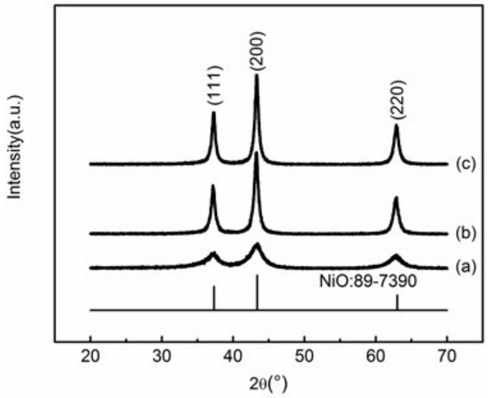

Fig. 5 Wide-angle XRD patterns of (a) NiO-40, (b) NiO-80 and (c) NiO-130.

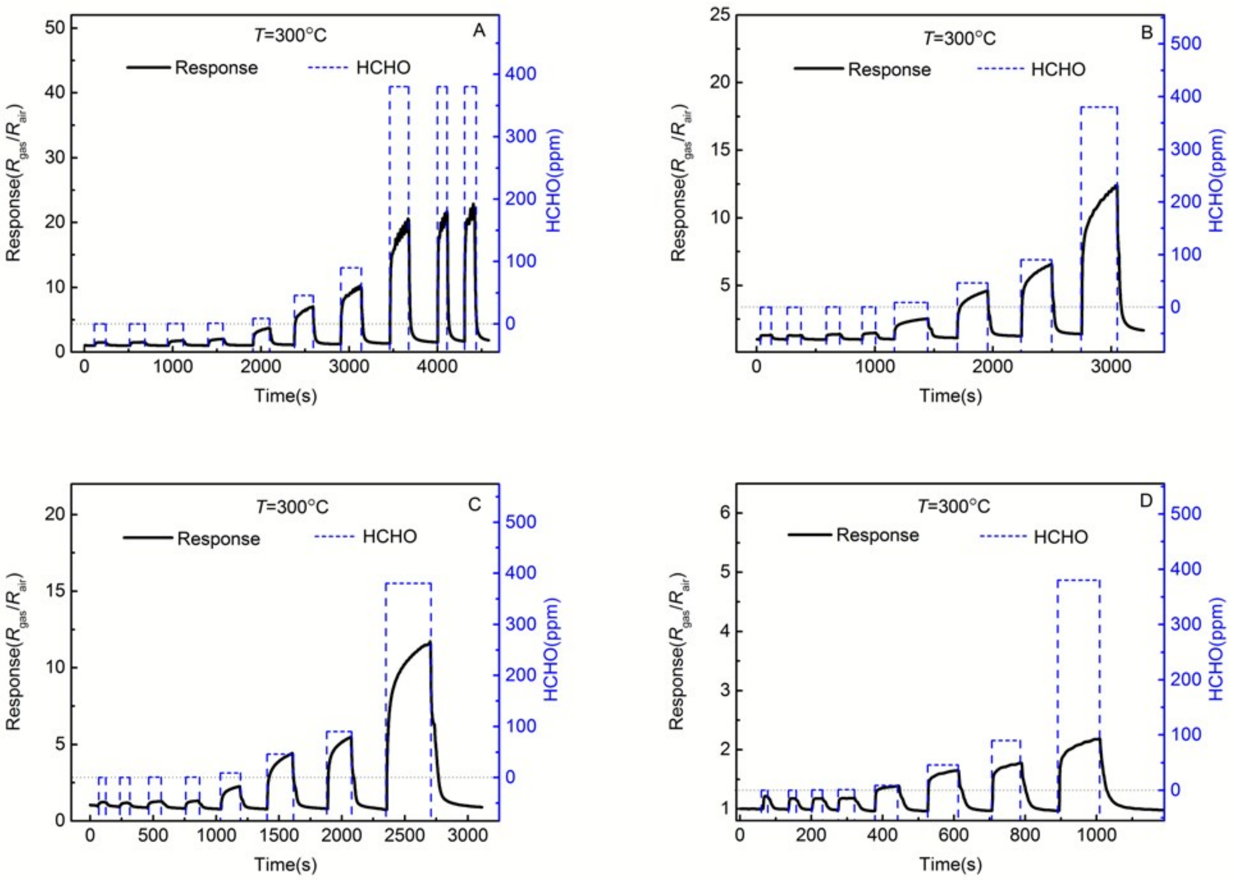

Fig. 6 Typical dynamic response curves of gas sensors fabricated from (A) NiO-40, (B) NiO-80, (C) NiO-130 and (D) bulk NiO particle, during cycling between increasing concentration of HCHO and ambient air at 300 °C.

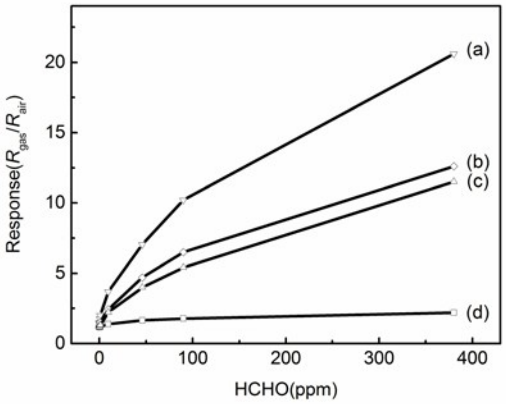

Fig. 7 Response versus HCHO concentration of gas sensors fabricated from (a) NiO-40, (b) NiO-80, (c) NiO-130, (d) bulk NiO particle.

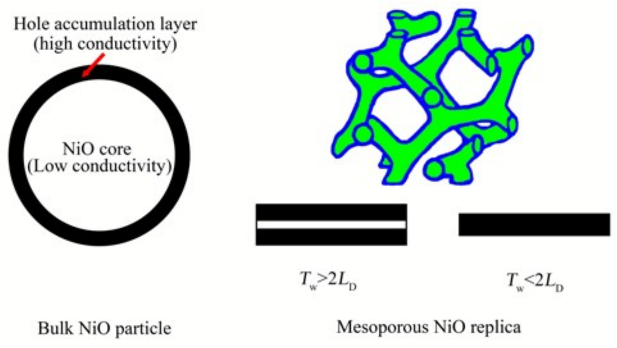

Fig. 8 Illustration of the dependence of the response on the textural parameters of the sensing material.